Thiourea Bismuth Iodide: Crystal structure, Characterization and High Performance as an Electrode Material for Supercapacitors

DOI: 10.1002/ ((please add manuscript number)
Article type: Full Paper

Thiourea Bismuth Iodide: Crystal structure, Characterization and High Performance as an Electrode Material for Supercapacitors

*Tianyue Li, John Mallows, Keir Adams, Gary S. Nichol, Job H. J. Thijssen and Neil Robertson.**

Tianyue Li, Dr. John Mallows, Keir Adams, Dr. Gary S. Nichol and Prof. Neil Robertson
School of Chemistry and EaStCHEM,
University of Edinburgh, King's Buildings
David Brewster Road
Edinburgh
EH9 3FJ
UK.
E-mail: neil.robertson@ed.ac.uk

Dr. Job H. J. Thijssen
SUPA School of Physics & Astronomy,
University of Edinburgh
Edinburgh
EH9 3FD
UK

Keywords: supercapacitors; electrode materials; iodobismuthates; zero-dimensional; solution-processable.

This paper reports on the synthesis, crystal structure and application of a novel hybrid bismuth-halide complex: $(CN_2SH_5)_3BiI_6$ (TBI) for supercapacitor applications, featuring merits including high areal capacitance, low cost, solution-processability and non-toxicity. Single crystal X-ray diffraction reveals that TBI crystallizes in the monoclinic system, with discrete $[BiI_6]^{3-}$ octahedra as the inorganic motif. Utilizing TBI as the active supercapacitor electrode material with carbon cloth current collector and aqueous $NaClO_4$ electrolyte, an electrode areal capacitance of 3.32 F/cm^2 and a systemic specific capacitance of 1030 F/g was achieved when the device operates as an electric double-layer capacitor (EDLC). The supercapacitor device shows excellent capacitance retention even after 5,000 charge-discharge cycles. The powder XRD patterns, Raman spectroscopy and SEM images of TBI electrodes were compared before and after the cycling test to demonstrate the material stability and investigate the film morphology.

1. Introduction

Supercapacitors are essential components of future energy storage systems as they possess high power density, quick charge-discharge rates and long cycle life, making them complementary to batteries and fuel cells.[1] Supercapacitors have a relatively simple design, are lightweight and suitable for a range of applications from circuitry and portable electronics to electric vehicles.[2] There are two types of capacitance mechanisms which can contribute to the overall capacitance of a supercapacitor. The first is the electric double layer capacitance (EDLC) caused by electrostatic charge accumulation at the electrode-electrolyte interface, which strongly relies on the accessibility of large electrode surface areas to the electrolytic ions.[3] The second is pseudocapacitance, which is a Faradaic electrochemical redox method of charge storage often observed in metal oxides or conducting polymers.[4] Pseudocapacitance may be higher by a factor of 100 than double-layer capacitance with the same electrode surface, however, the operational timescale is generally much lower, and can also induce more stability issues when compared to EDLCs. It therefore seems prudent to investigate a range of potentially suitable materials which are low-cost, stable and good charge conductors.[5]

Organic-inorganic halide perovskites are a class of materials which have recently been shown to be suitable in a range of applications such as photovoltaics, LED's, FET's and sensors amongst others.[6] These hybrid perovskites are three-dimensional materials with a general formula AMX_3, where A is a cation such as methylammonium, M is a metal cation such as Pb^{2+} and X is a halide anion. The most commonly reported hybrid perovskite is methylammonium lead iodide (MAPI), which has been highly studied in recent years particularly with regard to its use in high efficiency solar cells as a light absorbing layer with high ionic and electrical conductivity.[7] The need for low cost materials that can be printed from solution and show tuneable properties calls for further investigations into this type of functional material.[8] There are many reports of these materials tested for use in devices such as solar cells, but only a handful for use as redox active materials in supercapacitors. Zhao *et al.* previously reported a $MAPbI_3$-based thin-film device with an areal capacitance of 5.89 μF cm^{-2},[9] while Nair *et al*. recently reported the use of a lead-free methylammonium bismuth iodide (MBI) with a zero-dimensional crystal structure for

use in a supercapacitor, yielding an areal capacitance of 5.5 mF cm^{-2}.[10] Bismuth iodide perovskite-like materials have additional advantages compared to $MAPbI_3$ and other lead-halide perovskites such as non-toxicity, air-stability and moisture stability.[11] Despite these advantages however, MBI remains to date the only example studied. We report here on the synthesis and crystal structure of a novel hybrid iodobismuthate, thiourea bismuth iodide (TBI). Utilizing solution-processed TBI as the electroactive material in supercapacitors, we have achieved over three orders of magnitude increase in electrode areal capacitance compared to the previous work on MBI,[10] by optimising the electrode material, deposition method and electrolyte solution. Further investigations reveal the promise of TBI as a high performing, low-cost, eco-friendly and stable electrode material for supercapacitor applications.

2. Results and Discussion

2.1. Single crystal X-ray diffraction

TBI was synthesised by dissolving thiourea iodide with bismuth (III) iodide at 3:1 ratio in HI solution, and recrystallization by vapour diffusion from pentane. Single dark orange block-shaped crystals of TBI, with dimensions of (0.42×0.23×0.13) mm^3, were used for X-ray diffraction. TBI crystallised in the monoclinic crystal system with space group of $P2_1/c$. **Table S1** shows the main crystallographic data, with detailed information on bond length and angles available in **Figure S1** and **Table S2-3**. Isolated $[BiI_6]^{3-}$ octahedra comprise the inorganic entity of the crystal structure, showing a zero-dimensional crystal structural motif (**Figure 1a**). The $[BiI_6]^{3-}$ octahedron is distorted, with Bi-I bond lengths ranging from 3.3453 (8) Å to 2.9211 (9) Å, and the I-Bi-I angles ranging from 84.55 (2)° to 94.93 (3)°. The sulfur atom is protonated in the thiourea cation, and the S-C-N bond angles fall into the range of 115.7(8)° to 122.6(9) °, showing distortion from the ideal carbon sp^2 hybridization. This distortion has been reported in previous studies of $(NH_2)_2CSH^+$ cations [12], and in this case, it is potentially caused by the short contact distances between the protonated thiourea and the surrounding $[BiI_6]^{3-}$ octahedra. (**Figure S1**, **Figure 1b**)

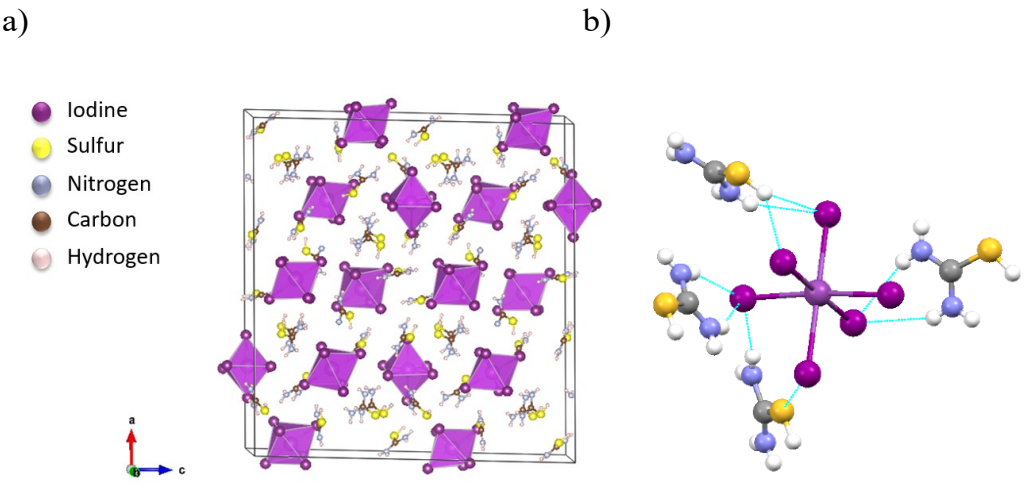

Figure 1 (a) Schematic diagram of a TBI unit cell viewed along the b axis. The unit cell boundary is marked with dark lines. Bismuth iodide octahedra are shown in magenta. The figure was generated from Vesta software [13]. (b) Short contacts (blue dashed lines) of the $[BiI_6]^{3-}$ octahedron with its surrounding protonated thiourea molecules. The figure was generated from Mercury software [14].

2.2 Electrode preparation and characterization

Electrodes based on TBI were fabricated via a solution-processing method, in which TBI was dissolved in DMF and mixed together with activated charcoal to enhance conductivity and PTFE to enhance mechanical integrity of the electrode surface (85:10:5 weight ratio). The suspension was deposited evenly onto carbon cloth, which is used as the charge collecting substrate. Excess solution was removed by an absorbing tissue placed underneath the electrode. TBI crystallizes upon heating the carbon cloth substrate at 150°C for 1 hour on a hotplate to remove the solvent. Pictures of an as-formed TBI electrode are presented in **Figure S2a**. The as-deposited TBI electrode was characterized by powder XRD, and compared with the calculated powder XRD pattern from the single crystal structure as shown in **Figure 2.** The as-deposited solution-processed TBI electrode shows a good peak position match with the theoretical pattern, with corresponding peaks for the (1 1 2), (2 0 4) and (6 0 6) planes. A broad peak across 23 - 29° on the 2θ scale is attributed to the carbon fibre substrate. Due to an insufficient amount of TBI material in this thin-film

form, BET isotherm surface area analysis is not feasible. We therefore also explored the surface morphology by SEM measurements. **Figure 3** presents the SEM images of solution-processed and, for comparison, suspension-processed TBI electrodes, giving insight into the crystallite size and coverage. We attempted to apply ImageJ software for crystallite size distribution analysis, however, due to the varies shapes and the merging / overlapping of the crystallites, the boundary of crystallites cannot be determined by the software. Nevertheless, it is clearly observable that more carbon cloth fibres are exposed in the suspension-deposited TBI electrodes, despite the fact that a similar amount of material was deposited onto the carbon cloth. This is caused by the aggregation of pre-formed TBI crystallites when using the suspension-deposited method. In contrast, the solution-processing results in higher surface coverage while minimizing the aggregation. The advantage of using a solution-processed electrode preparation method has also been investigated and proven in our previous work.[15] This enhanced coverage of TBI crystallites is anticipated to increase the charge storage ability, and therefore improve the capacitance of the device.

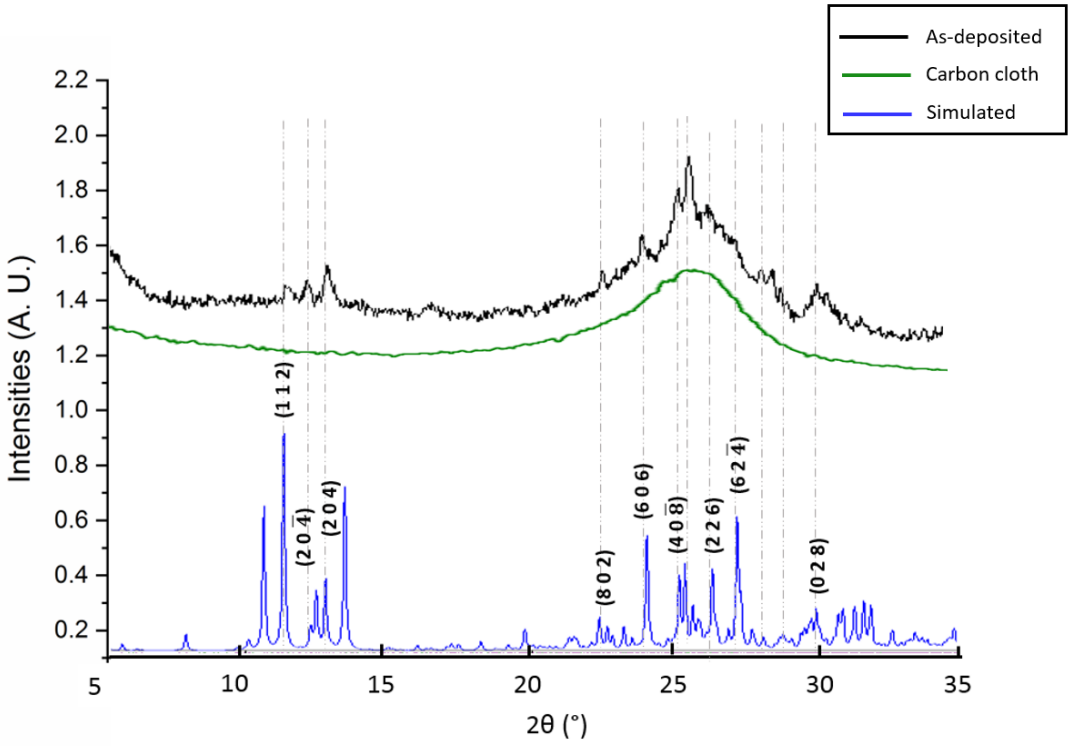

Figure 2. Powder XRD patterns of TBI as-deposited on carbon cloth (black), pure carbon cloth (olive) and the simulated powder XRD pattern by Mercury software (blue).[14]

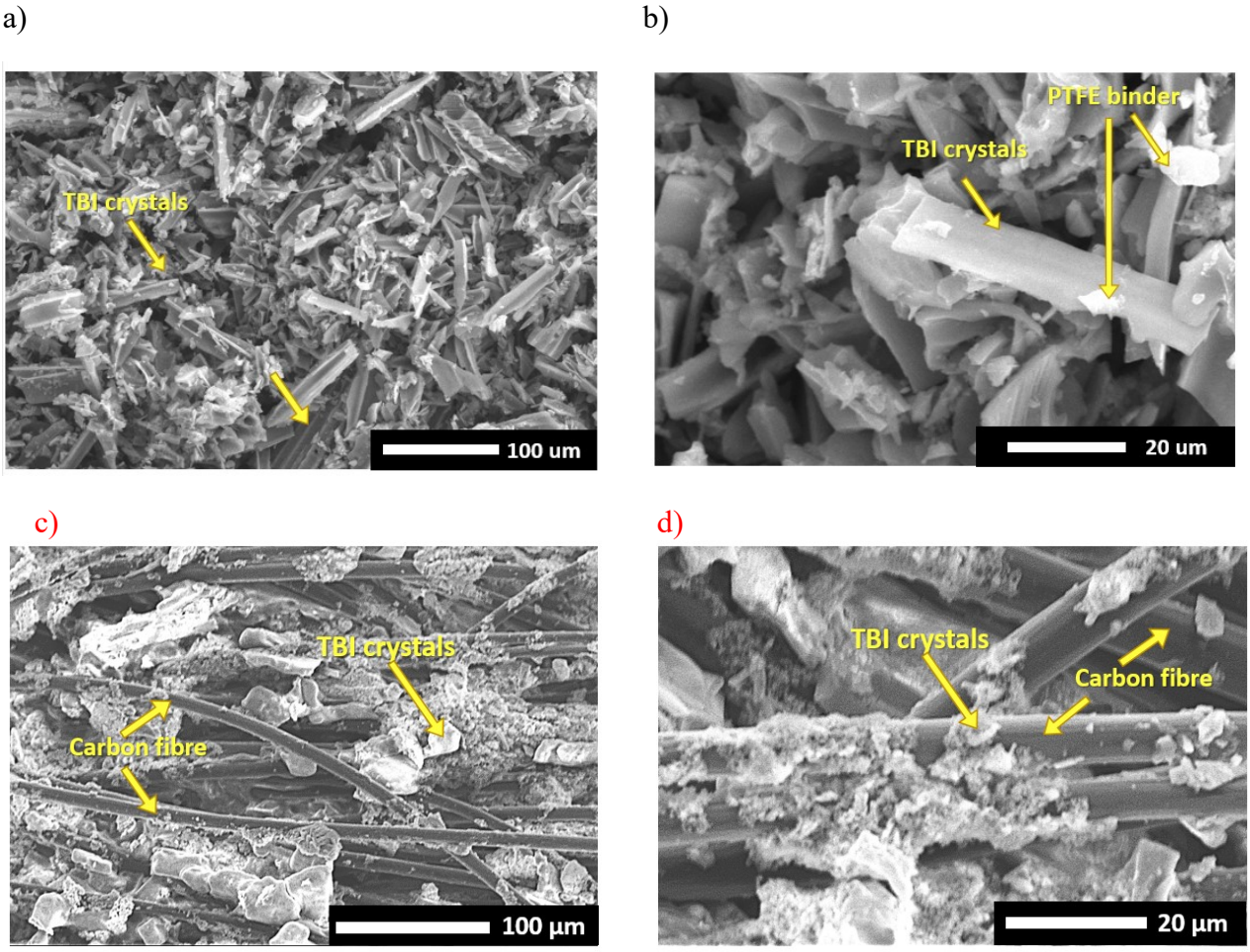

Figure 3. SEM images of as-deposited electrodes with solution-processed (a) (b) and suspension-processed (c) (d) TBI on carbon cloth substrate.

2.3 Device and charge storage mechanism studies and long-term cycle stability

To construct the supercapacitor device, a membrane separator was soaked in saturated $NaClO_4$ electrolyte solution before being sandwiched between two TBI coated carbon cloth electrodes. For better reproducibility and ease of measurement, the entire device was compressed in a standard test cell to give a firmly packed architecture. (**Figure 4**) The TBI-based supercapacitor performance was examined using both cyclic voltammetry (CV) and galvanostatic charge-discharge measurements. Varying the time and applied voltage/current density regimes during the measurements allowed the evaluation of the capacitive performance and analysis of the charge storage mechanism.

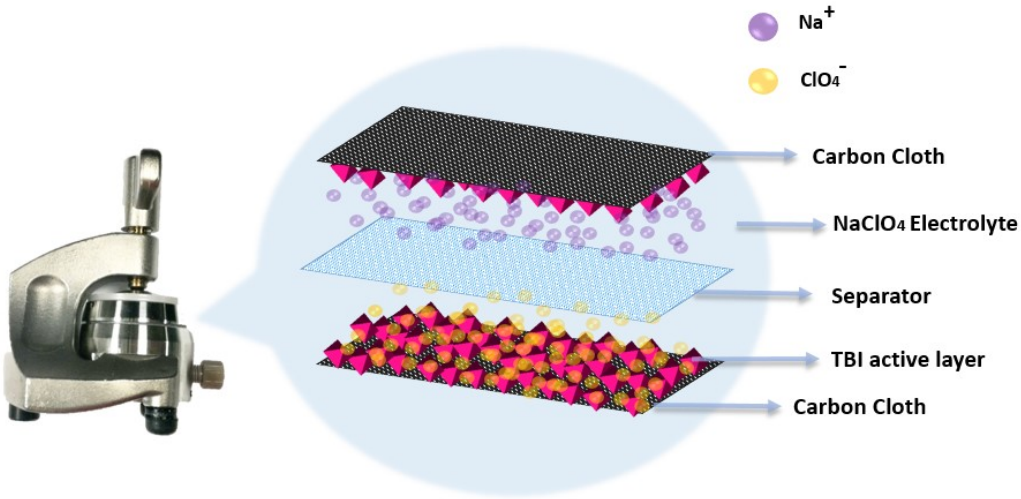

Figure 4. Schematic diagram of a TBI-based supercapacitor device that is compressed in a standard test cell.

The CV study was conducted in a voltage window of 0.0 – 0.6 V with a linear scan rate that varies from 0.01 V s^{-1} to 0.5 V s^{-1}, and **Figure 5a** depicts the CV curves measured at different scan rates. When a fast scan rate (0.5 V s^{-1}) is applied to the device, a rapid increase in the curent density versus potential gives an oval-shaped curve. The large slope of the charging onset indicates a strong resistive response from the device. This is mainly caused by insufficient time for Na^+ and ClO_4^- ions to diffuse to the electrode surface. Consequently, the fast scan rates cause the current to flow through the device in a resistive manner. As the sweep rate is reduced, more rectangular-shaped cuves can be obtained from the CV scans as the resistive effect caused by insufficient operating time is gradually minimized. The rectangular shaped CV curves, with a peakless plateau, indicate an effectively pure EDLC charge storage mechanism, where Na^+ and ClO_4^- ions diffuse and are stored in the micro-sized pores on the electrode surface through electrostatic interactions. The areal capacitance and specifc capacitance obtained from CV measurement was calculated according to Equation (1) and (2) [16]:

$$C_{areal} = \frac{\int_{\Delta V} i\, dV}{\Delta V \times s \times A} \qquad (1)$$

$$C_{specific} = \frac{\int_{\Delta V} i\, dV}{\Delta V \times s \times m} \qquad (2)$$

where $\boldsymbol{\Delta V}$ is the voltage range (V), i is the cathodic current (A), s is the scan rate (V s^{-1}), A is the geometric area for both of the electrodes (cm^2) and m (g) is the total mass of TBI coated on the

carbon cloth. The capacitance results under different scan rates are summarized in **Table S4**. The measured systemic capacitance increased from 23.7 mF cm^{-2} to 87.2 mF cm^{-2} (14.7 F g^{-1} to 87.2 F g^{-1}) as the scan rate decreased from 0.50 V s^{-1} to 0.01 V s^{-1}, showing that the scan rate interplays with the charge storage ability of the supercapacitor device.[17] Note that the areal capacitance from Equation (1) is the systemic capacitance of the whole device; for comparison we have also listed the electrode areal capacitance for each electrode in **Table S4** (i.e., double the systemic capacitance).

Galvanostatic charge-discharge measurement was carried out in addition to CV, where the voltage of the capacitor is plotted against time during charge-discharge cycles under a constant current. The device was tested under different current densities (from 0.22 A g^{-1} to 1.74 A g^{-1}). Largely triangular charge-discharge curves can be observed, particularly at higher current density, showing typical capacitative behaviour. However, a non-constant slope of the charge-discharge curve can be observed when lower current density is applied during the measurement. Initially upon charging, a steep onset can be found under the 10s time scale, showing fast charge storage at the easily-accesible electrode surface. This is followed by a less steep charging curve, as the longer time regime (over 10s) allows the ions to diffuse into the kinetically-limited deeper holes. As charges cover the full surface of both electrodes, the charge storage is saturated, represented by the flatening curve. During the discharge process, rapid potential drop is again attributed to the device internal resistance, followed by release of both electrostatically stored easily-accessible surface charge and kinetically-limited charge release. The relationship between applied current density and iR drop is shown in **Figure S3**. Such asymmetry of charge-discharge curves can also be found in the literature, however, the decrease of coulumbic efficiency under lower current density implies irreversable electrochemical process over long discharging time. 3b, [10] The areal and specific capacitances based on galvanostatic measurement were calculated according to Equation (3) and (4), respectively.[16]

$$\boldsymbol{C_{areal}} = \frac{\boldsymbol{i}}{\frac{\boldsymbol{dV}}{\boldsymbol{dt}} \times \boldsymbol{A}} \qquad (3)$$

$$\boldsymbol{C_{specific}} = \frac{\boldsymbol{i}}{\frac{\boldsymbol{dV}}{\boldsymbol{dt}} \times \boldsymbol{m}} \qquad (4)$$

where i is the constant current applied to the measurement (A), $\frac{dV}{dt}$ is the slope of the discharge curve (V/s), A is the geometric area for both of the electrodes (cm^2) and m is the total mass of TBI coated on the carbon cloth (g). As the applied constant current density decreases from 1.44 A g^{-1} to 0.22 A g^{-1}, the measured capacitance increased from 941 mF cm^{-2} to 1450 mF cm^{-2} (586 F g^{-1} to 899 F g^{-1}), reaching a systemic peak capacitance of 1660 mF cm^{-2} (or 1030 F g^{-1}) under a constant current of 0.44 A g^{-1}. Narrower voltage windows were chosen for the measurements under 0.22 A g^{-1} and 0.44 A g^{-1}, where the device was switched to discharging mode when a charging plateau is approaching, to avoid a mechanism switch to a Faradaic process. At the same time, the charge-discharge cycle time is approximately inversely-proportional to the applied current density, which to a large extent influences the charge storage mechanism as discussed above. This can be readily illustrated by plotting the instantaneous capacitance based on different points on the discharge curve, whereby the differential is taken and calculated according to Equation 3 and 4, with results in **Figure 5c**. The above capacitance values were calculated based on the slope of discharging curve at the maximum point in Figure 5c. For complete information, the average capacitrance values calculated based on the total discharge time are tabulated in Table S4b.

The long-term stability of the TBI supercapacitor device is proven experimentally by cyclic voltammetry, showing no capacitance loss after 5000 charge-discharge cycles (**Figure 5d**). The initial increase of capacitance is attributed to the modification and surface rearrangement of the electrode material surface and/or morphology during cycles under the charging-discharging environment, which can also explain the discrepancy between the CV curve shape of the 1st cycle and 5000th cycle (**Figure S4**). The powder XRD pattern of the TBI electrode after 5000 cycles however, shows mainly the heavily $NaClO_4$ coated carbon cloth, making it difficult to compare with the theoretical pattern (**Figure S2b, c, d; S5a**). Therefore, to further demonstrate the material stability under cycle testing, we carried out Raman spectroscopy measurements. The Raman spectra of the TBI electrodes before/after 5000 cycles show no substantial changes regarding the Bi-I vibrational modes, however, higher background noise was observed for the electrode after cycing, which again may be attributed by $NaClO_4$ coating (**Figure S5b**). In this initial assessment

of the new material, CV cycling was used as a rapid and straightforward method for the stability testing ensuring the device is operating under an EDLC mechanism. Since reduced coulombic efficiency was observed in the galvanostatic charge-discharge measurement however, we note that slower galvanostatic measurements for the cycling test may lead to lower stability due to a longer timescale.

Using $NaClO_4$ as the electrolyte and TBI as the active electrode material with an optimized solution-processed deposition method, we have achieved over 600 times higher (electrode) areal capacitance compared to the previous work on a similar 0D hybride iodobismuth material[10], and over 5 orders of magnitude higher than the study on a 3D lead-halide perovskite [9].

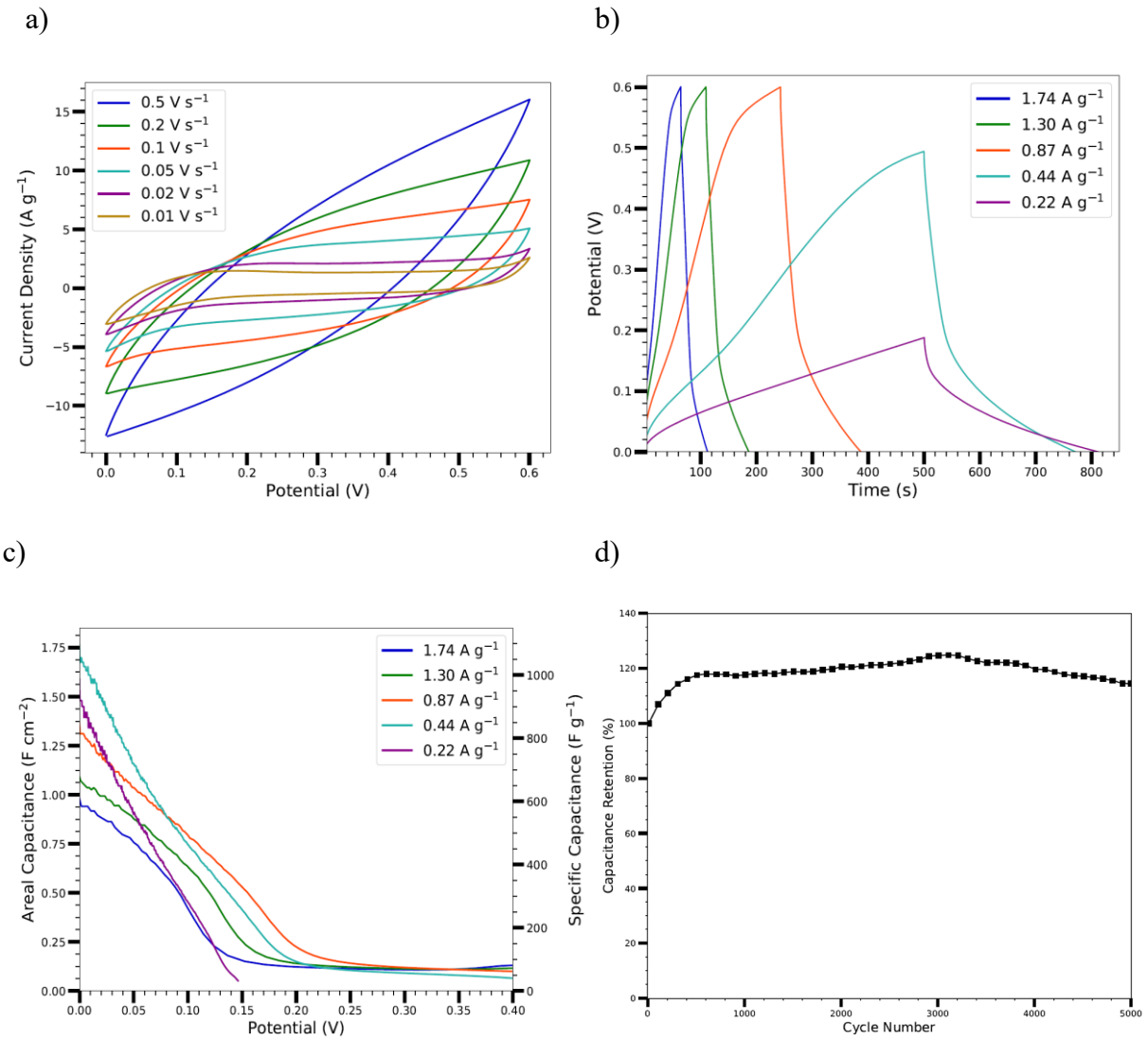

Figure 5. (a) Cyclic voltammograms of the supercapacitor measured at different scan rate. (b) Galvanostatic charge-discharge curves measured at varies current densities. (c) Instantaneous areal capacitance of the supercapacitor versus the potential based on galvanostatic charge-discharge

measurement. (d) Capacitance retention of the TBI – based supercapacitor tested for 5000 CV cycles at a scan rate of 0.1 V s^{-1}.

2.4 Electrochemical impedance spectroscopy and equivalent circuit

To further investigate the device operation and charge storage mechanism, electrochemical impedance spectroscopy (EIS) measurements were carried out under AC potential to probe the equivalent circuit of the device. [18] In this study, the circuit response under applied frequency ranging from 0.01 Hz to 150 kHz was collected with an amplitude of ±10 mV at open circuit potential (OCP). **Figure 6a** depicts the in-phase versus out-of-phase impedance (Nyquist plot) of a TBI-based supercapacitor at OCP of 0 V, and **Figure 6b** shows the frequency response of the circuit, known as Bode plot. Based on the above two plots, we probed the equivalent circuit (inserted in **Figure 6a**) to simulate the physical processes in the supercapacitor device. In the high frequency region, the high oscillation leads to insufficient time to form the double layer, leading to a more resistive response in the circuit. This is simulated as the bulk resistance (R_1) corresponding to the resistance from the $NaClO_4$ electrolyte and carbon cloth current collector, with a value of 1.137 Ω matching the interception of the Nyquist curve on the Z' axis. The first semicircle on the Nyquist plot is attributed to the charge transfer process between the electrode active material and current collector. Due to the intrinsically low density of states of carbon cloth, the contact capacitance is non-zero and can be simulated by a constant Q_1 phase element (CPE) of 2.057 μF with an ideality factor of 0.7554, demonstrating a small capacitance contribution to the circuit [19]. In parallel with Q_1, the charge transfer resistance R_2 is simulated to be 5.47 Ω from the equivalent circuit, showing negligible discrepancy from the diameter of the 1st semicircle on the Nyquist plot. The sum of R_1 and R_2 is known as the internal resistance, which corresponds to the resistance calculated from the iR drop in galvanostatic charge-discharge measurement.[20] The capacitance attributed to electrostatically stored charges in easily-accessible surface sites is simulated as Q_2, which is in parallel with device leakage resistance R_3.[19b] The dominant capacitive behavior is simulated as another CPE (Q_3), with a capacitance of 0.7063 F and an ideality factor of 0.9007. This is attributed to the capacitative charge-storage behavior of the full material surface, broadly consistent with the specific capacitance (0.7373 F) from the

Galvanostatic charge-discharge measurement, with a small discrepancy due to the AC measurement environment. The values and errors of each simulated circuit element are summarized in **Table 1**. The EIS measurement and equivalent circuit analysis for the device after 5000 cycles stability test was also carried out as shown in **Figure S6**, with the values of equivalent circuit elements tabulated in **Table S5**. The imaginary impedance (Z'') versus frequency before and after the cycling stability test is presented in **Figure S7**, showing a decreased out-of-phase component when compared to the as-prepared TBI supercapacitor. The same equivalent circuit can be simulated, however, a smaller series resistance value but larger charge transfer resistance values were observed for the post-cycled device, attributed to some minor modification of the material surface through ionic diffusion and interaction during cycles.

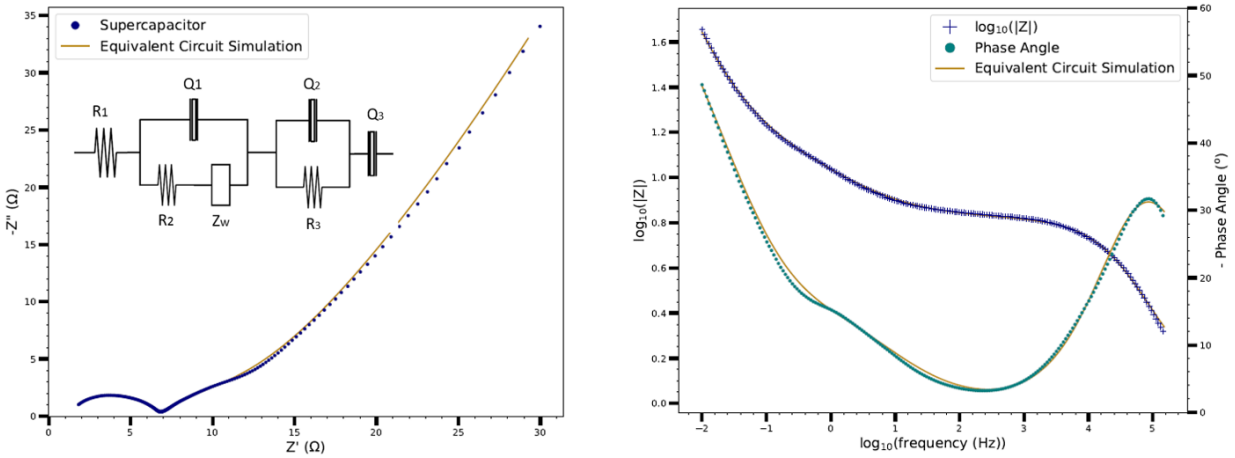

Figure 6. (a) Nyquist plot of a TBI-based supercapacitor (blue) with fitted curve based on simulated circuit (yellow); simulated equivalent circuit diagram is inserted. (b) Bode plot of a TBI-based supercapacitor showing absolute impedance (blue), phase angle (green) with fitted curve based on equivalent circuit (yellow).

Table 1 Summary of the values and errors (%) of equivalent circuit elements.

Circuit Element	Value	% Error
R_1	1.137 Ω	8.433
$Q_1 - \boldsymbol{n}$	0.7554	1.857
$Q_1 - Y_0$	2.057 μF	13.787
R_2	5.47 Ω	2.005
$Q_2 - \boldsymbol{n}$	0.5642	1.502
$Q_2 - Y_0$	0.0737 F	3.200
R_3	4.28 Ω	5.330

$Q_3 - \boldsymbol{n}$	0.9007	0.311
$Q_3 - Y_0$	0.7063 F	0.810
Z_w	0.1775 Ω^{-1} $s^{1/2}$	4.357

3. Conclusion

A novel organic-inorganic iodobismuthate material: TBI, has been synthesized and studied as a stable electrode material for supercapacitor applications. TBI crystallizes in a monoclinic crystal system, featuring 0D isolated $[BiI_6]^{3-}$ octahedra and S-site protonated thiourea cations. Using carbon cloth as the current collector and aqueous $NaClO_4$ solution as the electrolyte, we fabricated low-cost and stable TBI-based supercapacitor devices and investigated the charge storage mechanism by cyclic voltammetry, galvanostatic charge-discharge measurement and EIS. A maximum electrode areal capacitance over 3.32 F/cm^2 and a systemic specific capacitance over 1030 F/g have been achieved, which is 600 times higher capacitance than the only literature precedents of similar materials. Excellent capacitance retention was achieved, and the cycling stability of the active material was examined by Raman spectroscopy. The enhanced device performance is attributed to our solution-processed electrode material preparation method, leading to excellent surface coverage with highly crystalline TBI-based electrodes. The outstanding capacitive performance with pH neutral $NaClO_4$ electrolyte and long-term cycling stability prove TBI to be a suitable electrode material for supercapacitor applications.

4. Experimental Section

4.1 Materials

All of the chemicals were purchased from Sigma Aldrich and used as received, unless otherwise stated: N, N-Dimethylformamide (anhydrous, 99.8%), bismuth(III) iodide (powder, 99%), poly(tetrafluoroethylene) (powder with 1 μm particle size), activated charcoal (CAS: 7440-44-0), Thiourea (≥99%), hydroiodic acid (57 wt% in water, stabilized, 99.95%). Thiourea iodide salt was prepared from 1:1 stoichiometry of thiourea and HI in ethanol/water solvent, and the product was synthesized after stirring at room temperature overnight, followed by rotary evaporation of solvent, washing with diethyl ether and drying under vacuum (yield: 96.8%). ^{1}H

NMR was carried out in deuterated oxide (D_2O) for thiourea iodide on a Bruker Advance Pro500 spectrometer and referenced externally to $SiMe_4$.

4.2 Single crystal study of TBI

TBI precursor solution was prepared by dissolving thiourea iodide with bismuth iodide at 3:1 ratio in HI solution, and single dark orange block-shaped crystals of TBI were recrystallized by vapour diffusion from pentane. A suitable crystal (0.42×0.23×0.13) mm^3 was selected and mounted on a MITIGEN holder in Paratone oil on a Rigaku Oxford Diffraction SuperNova diffractometer. The crystal was kept at T = 120.0 K during data collection. Using Olex2 [19], the structure was solved with the ShelXS structure solution program, using the Direct Methods solution method.[21] The model was refined with version 2017/1 of ShelXL using Least Squares minimisation.[22]

4.3 Electrode preparation

The electrode material precursor suspension was prepared by mixing 80.8 mg thiourea iodide, 78.63 mg of BiI_3, 18.75 mg of activated charcoal and 9.38 mg of PTFE powder in 1 mL DMF, which was then sonicated for 1 hour. The carbon cloth (NuVant Systems Inc., ELAT Hydrophilic) was cut with 1 cm x 1 cm dimensions and placed on top of an absorbing tissue before being deposited with 200 μL of the electrode material suspension. The soaked carbon cloth was then placed in a petri-dish and heated at 150 ºC for 1 hour to remove the solvent and facilitate the TBI crystallization process. The dried electrode was then trimmed, weighed and geometrically measured under an optical microscope. The two symmetrical electrodes used in this study have dimensions of 0.89 cm x 0.95 cm and 0.95 cm x 0.94 cm, and the active material mass is calculated by subtracting the mass of carbon cloth (calculated from the density) from the total mass of the dried electrode, yielding in 0.609 mg and 0.791 mg, respectively.

4.4 Supercapacitor fabrication

To assemble the TBI-based supercapacitor, a circular thin microporous polymer membrane (Celgard 3501, 25 μm) was sandwiched between two as-prepared electrodes after being soaked in a saturated aqueous $NaClO_4$ electrolyte solution. The electrode/separator/electrode stack was then

packed into an electrochemical cell (ECC-std, EL-CELL GmbH) and tightly compressed to minimize separation between the two symmetrical electrodes.

4.5 Electrochemical measurement

Electrochemical analysis was performed by connecting the supercapacitor test cell in a two-electrode configuration to an Autolab potentiostat with an FRA2 module. Cyclic voltammetry was performed in the voltage window of 0 to 0.6 V at scan rates ranging from 0.01 V/s to 0.5 V/s. Galvanostatic charge-discharge measurements were conducted under different constant current densities, with the discharging process taking place when reaching either the pre-set potential (0.6 V) or a maximum measurement time (800 s). The current densities are reported with respect to the average mass of active material on both electrodes. Both measurements were carried out using the General Purpose Electrochemical System software (GPES, version 4.9.007). Electrochemical impedance spectroscopy was carried out using Frequency Response Analyser (FRA, version 4.9.007) software with a frequency ranging from 0.01 Hz to 150 kHz. Equivalent circuit fitting was conducted using FRA's Fit and Simulation software (version 1.7).

4.6 Electrode characterization

Powder X-Ray diffraction was conducted on a Bruker (D2 Advance) diffractometer utilizing monochromatic Cu-Kα radiation (wavelength 1.5406 Å) at room temperature. XRD scans were performed at scattering angles ranging from 5º to 50º with 0.05º increments on a 2-theta scale. Raman spectroscopy was performed using a Renishaw InVia Raman Microscope (wavelength 785 nm, spectral resolution 1 cm^{-1}). SEM images were acquired using a JEOL JSM-6010PLUS/LV scanning electron microscope, with an electron beam accelerating voltage of 10 kV using secondary electron imaging. Carbon cloth mounted with active material was placed directly onto a sticky carbon pad on an SEM sample holder.

[CCDC 1872987 contains the supplementary crystallographic data for this paper. These data can be obtained free of charge from The Cambridge Crystallographic Data Centre via www.ccdc.cam.ac.uk/data_request/cif.]

5. Conflicts of interest

There are no conflicts of interest to declare.

6. Supporting Information

Supporting Information is available from the Wiley Online Library or from the author.

7. Acknowledgements

We thank the EPSRC Multiscale Tuning of Interfaces and Surfaces for Energy Applications consortium for a flexible-funding project (Open data at: https://doi.org/10.7488/ds/2501), and the School of Chemistry, University of Edinburgh for financial support. We thank EPSRC SOFI CDT for access to SEM and Dr. Andrew Schofield for help with SEM measurements. We thank Dr. Andrey Gromov for help with the Raman measurements. We thank Dr. Dimitrios Kampouris for fruitful discussion about the supercapacitor studies. KA thanks the University of Chicago/University of Edinburgh student exchange scheme for support.

8. References

[1] M. Cakici, R. R. Kakarla, F.Alonso-Marroquin, *Chem. Eng. J.* **2017**, 309, 151-158.

[2] K. Li, J. Liu, Y. Huang, F. Bu, Y. Xu, *J. Mater. Chem. A*, **2017**, 5, 5466-5474.

[3] K. Jost, G. Dion, Y. Gogotsi, *J. Mater. Chem. A,* **2014**, 2, 10776-10787. b) T. Purkait, G. Singh, D. Kumar, M. Singh and R.S. Dey, *Sci. Rep*., **2018**, 8, 640.

[4] a) Y. Zhang, H. Feng, X. Wu, L.Wang, A. Zhang, T. Xia, H. Dong, X. Li, L. Zhang, *Int. J. Hydrog. Energy,* **2009**, 34, 4889-4899. b) W. Fang, N, Zhang, L. Fan, K. Sun, *J. Power Sources,* **2016**, 333, 30-36. c) Y. Zhang, L. Fan, P. Wang, Y. Yin, X. Zhang, N. Zhang, and K. Sun, *Nanoscale*, **2017**, 9, 17694-17698. d) C. Guan, W. Zhao, Y. Hu, Z. Lai, X. Li, S. Sun, H. Zhang, A. K. Cheetham and J. Wang, *Nanoscale Horiz.*, **2017**, 2, 99-105. e) X. Li, H. Wu, A. M. Elshahawy, L. Wang, S. J. Pennycook, C. Cuan, and J. Wang, *Adv. Funct. Mater.,* **2018**, 28, 1800036.

[5] G. Wang, L. Zhang, J. Zhang, *Chem. Soc. Rev.,* **2012**, 41 (2), 797-828.

[6] a) N. G. Park, T. Miyasaka, M. Grätzel, *Organic-Inorganic Halide Perovskite Photovoltaics, Springer*, Switzerland, **2016**; b) T. Li, Y. Hu, C. A. Morrison, W. Wu, H. Han, N. Robertson, *Sustainable Energy & Fuels,* **2017**, 1, 308-316; c) Y. H. Kim, H. Cho, J. H. Heo, T. S. Kim, N. Myoung, C. L. Lee, S. H. Im, T. W. Lee, *Adv. Mater.* **2015**, 27, 1248-1254. d) Y. Zhao, K. Zhu, *Chem. Soc. Rev.* **2016**, 45 (3), 655-689. e) T. Li, Q. Wang, G. S. Nichol, C. A. Morrison, H. Han and N. Robertson, *Dalton Trans.,* **2018**, 47, 7050-7058.

[7] a) T. Baikie, Y. Fang, J. M.Kadro, M. Schreyer, F. Wei, S. G. Mhaisalkar, M. Graetzel, T. J. White, *J. Mater. Chem. A,* **2013**, 1, 5628-5641. b) M. L.Petrus, J. Schlipf, C. Li, T. P. Gujar, N. Giesbrecht, P. Müller‐Buschbaum, M. Thelakkat, T. Bein, S. Hüttner, P. Docampo, *Adv. Energy Mater.,* **2017**, 7, 1700264.

[8] a) E. Mosconi, B. Merabet, D. Meggiolaro, A. Zaoui, F. De Angelis, *J. Phys. Chem. C,* **2018**, 122, 14107−14112. b) W. Li, Z. Wang, F. Deschler, S. Gao, R. H. Friend, A. K. Cheetham, *Nat. Rev. Mater.,* **2017**, 2 (3), 16099.

[9] S. Zhou, L. Li, H. Yu, J. Chen, C. P. Wong, N. Zhao, *Adv. Electron Mater.* **2016**, 2, 1600114.

[10] J. K. Pious, M. Lekshmi, C. Muthu, R. Rakhi, C. Nair, *ACS Omega*, **2017**, 2 (9), 5798-5802.

[11] a) M. Lyu, J.-H. Yun, M. Cai, Y. Jiao, P. V. Bernhardt, M. Zhang, Q. Wang, A. Du, H. Wang, G. Liu, *Nano Research* 2016, 9 (3), 692-702. b) W. Lu, L.Dai, *Carbon Nanotube,* InTechOpen, London, UK **2010**, pp. 564-589.

[12] a) M. J. Janssen, *Spectrochimica Acta*, 1961, 17, 475-485. b) M. Li and R. K. Li, *Dalton Trans.,* 2014, 43, 2577. c) O. V. Rudnitskaya, E. K. Kultyshikina, E. V. Dobrokhotova, V. S. Podvoyskaya, P. V. Dorovatovskii, V. A. Lazarenko, Y. V. Zubavichus, V. Khrustalev, *Polyhedron,* **2017**, 134, 114-119.

[13] K. Momma and F. Izumi, *J. Appl. Crystallogr*., **2011**, 44, 1272-1276.

[14] C. F. Macrae, I. J. Bruno, J. A. Chisholm, P. R. Edgington, P. McCabe, E. Pidcock, L. Rodriguez-Monge, R. Taylor, J. van de Streek and P. A. Wood, *J. Appl. Cryst.,* **2008**, 41, 466-470.

[15] K. Adams, A. Franco Gonzalez, J. Mallows, T. Li, J. H. J. Thijssen and N. Robertson, *J. Mater. Chem. A,* **2019**, 7, 1638-1646.

[16] B. E.Conway, *Electrochemical Supercapcitors Scientific Fundamentals and Technological Applications,* Springer, USA, **1999**.

[17] J. Xie, P. Yang, Y. Wang, T. Qi, Y. Lei and C. M. Li, *J. Power Sources*, **2018**, 201, 213-223.

[18] E. Barsoukov, J. R. Macdonald, *Impedance Spectroscopy Theory, Experiment and Applications (2nd edition*), John Wiley & Sons, USA, **2018**.

[19] a) H. Ji, X. Zhao, Z. Qiao, J. Jung, Y. Zhu, Y. Lu, L. Zhang, A. H. MacDonald and R. S. Ruoff, *Nat Comm,* **2014**, 5, 3317. b) C. Lei, S Markoulidisa, Z. Ashitakab, C. Lekakoua, *Electrochimica Acta* **2013**, 92, 183– 187

[20] B. Mei, O. Munteshari, J. Lau, B. Dunn and L. Pilon, *J. Phys. Chem. C,* **2018**, 122 194-206

[21] a) O. V. Dolomanov, L. J. Bourhis, R. J. Gildea, J. A. K. Howard and H. Puschmann, *J. Appl. Crystallogr.*, **2009**, 42, 339-341.b) G. M. Sheldrick, *Acta Cryst. A*, **2008**, 64, 112-122.

[22] G. M. Sheldrick, *Acta Cryst.,* **2015**, C71, 3-8.

Supporting Information

Thiourea Bismuth Iodide: Crystal structure, Characterizations and Application as an Electrode Material for Supercapacitors

*Tianyue Li, John Mallows, Keir Adams, Gary S. Nichol, Job H. J. Thijssen and Neil Robertson.**

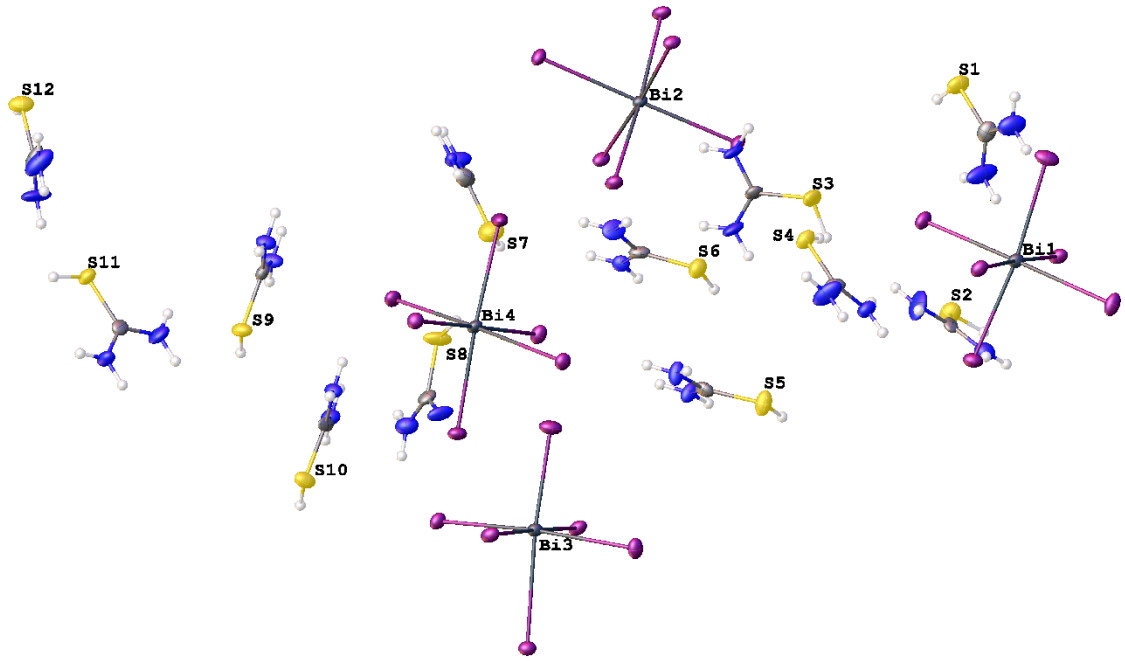

Figure S1. The asymmetric unit of TBI obtained from single crystal XRD. Displacement ellipsoids are at the 50% probability level.

Table S1. Crystallographic data for TBI

Formula	$C_3H_{18}BiI_6N_6S_3$
$D_{calc.}$/ g cm^{-3}	3.302
μ/mm^{-1}	15.172
Formula Weight	1204.79
Size/mm^3	0.42×0.23×0.13
T/K	120.0
Crystal System	monoclinic
Space Group	$P2_1/c$
a/Å	33.2403(4)

b/Å	9.44695(12)
c/Å	30.8920(4)
$\alpha/^{\circ}$	90
$\beta/^{\circ}$	91.8969(10)
$\gamma/^{\circ}$	90
V/Å^3	9695.4(2)
wR2 (all data)	0.1146
wR2	0.1047
R1 (all data)	0.0721
R1	0.0542

Table S2: Bond Lengths in Å for TBI.

Atom	Atom	Length/Å
Bi1	I1	3.0391(8)
Bi1	I2	3.0460(8)
Bi1	I3	3.1145(8)
Bi1	I4	3.1207(7)
Bi1	I5	3.0981(8)
Bi1	I6	3.0392(7)
Bi2	I7	3.0613(7)
Bi2	I8	3.0299(7)
Bi2	I9	3.1316(7)
Bi2	I10	3.1014(7)
Bi2	I11	3.0107(7)
Bi2	I12	3.0715(7)
Bi3	I13	3.0766(8)
Bi3	I14	2.9589(8)
Bi3	I15	3.3452(7)
Bi3	I16	3.0571(7)
Bi3	I17	3.2181(7)
Bi3	I18	2.9210(8)
Bi4	I19	3.1251(8)
Bi4	I20	3.0833(8)
Bi4	I21	3.2036(7)
Bi4	I22	3.0153(8)
Bi4	I23	3.0750(7)
Bi4	I24	2.9965(7)
S1	C1	1.734(12)
N1	C1	1.319(15)
N2	C1	1.293(14)
S2	C2	1.725(12)
N3	C2	1.316(14)
N4	C2	1.311(14)
S3	C3	1.748(11)
N5	C3	1.291(13)
N6	C3	1.314(14)
S4	C4	1.747(10)
N7	C4	1.322(14)
N8	C4	1.283(14)
S5	C5	1.731(11)
N9	C5	1.315(13)
N10	C5	1.308(13)
S6	C6	1.731(12)
N11	C6	1.332(14)
N12	C6	1.288(13)
S7	C7	1.680(12)
N13	C7	1.465(15)
N14	C7	1.299(15)
S8	C8	1.707(11)
N15	C8	1.314(14)
N16	C8	1.337(14)
S9	C9	1.745(11)
N17	C9	1.317(13)
N18	C9	1.308(13)
S10	C10	1.742(11)
N19	C10	1.317(14)
N20	C10	1.312(13)
S11	C11	1.718(11)
N21	C11	1.303(14)
N22	C11	1.322(14)
S12	C12	1.732(12)
N23	C12	1.303(16)
N24	C12	1.266(16)

Table S3: Bond angles in ˚ for TBI.

Atom	Atom	Atom	Angle/°
I1	Bi1	I2	89.25(2)
I1	Bi1	I3	86.62(2)
I1	Bi1	I4	175.70(2)
I1	Bi1	I5	91.56(2)
I1	Bi1	I6	89.74(2)
I2	Bi1	I3	94.63(2)
I2	Bi1	I4	91.24(2)
I2	Bi1	I5	173.37(2)
I3	Bi1	I4	89.08(2)
I5	Bi1	I3	91.99(2)
I5	Bi1	I4	88.44(2)
I6	Bi1	I2	86.85(2)
I6	Bi1	I3	176.05(2)
I6	Bi1	I4	94.55(2)
I6	Bi1	I5	86.57(2)
I7	Bi2	I9	85.73(2)
I7	Bi2	I10	86.64(2)
I7	Bi2	I12	173.62(2)
I8	Bi2	I7	94.93(2)
I8	Bi2	I9	89.19(2)
I8	Bi2	I10	175.81(2)
I8	Bi2	I12	89.86(2)
I10	Bi2	I9	87.049(19)
I11	Bi2	I7	93.89(2)
I11	Bi2	I8	91.65(2)
I11	Bi2	I9	179.10(2)
I11	Bi2	I10	92.11(2)
I11	Bi2	I12	90.18(2)
I12	Bi2	I9	90.13(2)
I12	Bi2	I10	88.30(2)
I13	Bi3	I15	85.43(2)
I13	Bi3	I17	89.60(2)
I14	Bi3	I13	93.33(2)
I14	Bi3	I15	89.93(2)
I14	Bi3	I16	91.13(2)
I14	Bi3	I17	176.31(2)
I16	Bi3	I13	173.09(2)
I16	Bi3	I15	89.31(2)
I16	Bi3	I17	85.74(2)
I17	Bi3	I15	88.069(19)
I18	Bi3	I13	90.14(2)
I18	Bi3	I14	92.50(2)
I18	Bi3	I15	175.07(2)
I18	Bi3	I16	94.93(2)
I18	Bi3	I17	89.73(2)
I19	Bi4	I21	89.73(2)
I20	Bi4	I19	89.74(2)
I20	Bi4	I21	94.91(2)

Atom	Atom	Atom	Angle/°
I22	Bi4	I19	178.60(2)
I22	Bi4	I20	90.81(2)
I22	Bi4	I21	88.93(2)
I22	Bi4	I23	94.58(2)
I23	Bi4	I19	84.86(2)
I23	Bi4	I20	174.58(2)
I23	Bi4	I21	84.55(2)
I24	Bi4	I19	89.36(2)
I24	Bi4	I20	87.54(2)
I24	Bi4	I21	177.37(2)
I24	Bi4	I22	91.96(2)
I24	Bi4	I23	92.92(2)
N1	C1	S1	116.8(9)
N2	C1	S1	121.5(10)
N2	C1	N1	121.7(11)
N3	C2	S2	119.3(9)
N4	C2	S2	119.4(9)
N4	C2	N3	121.3(11)
N5	C3	S3	117.2(8)
N5	C3	N6	122.5(10)
N6	C3	S3	120.3(8)
N7	C4	S4	115.6(8)
N8	C4	S4	121.9(9)
N8	C4	N7	122.6(10)
N9	C5	S5	118.2(8)
N10	C5	S5	121.4(8)
N10	C5	N9	120.3(10)
N11	C6	S6	119.5(8)
N12	C6	S6	120.1(9)
N12	C6	N11	120.4(11)
N13	C7	S7	112.7(8)
N14	C7	S7	119.5(10)
N14	C7	N13	127.7(11)
N15	C8	S8	122.5(9)
N15	C8	N16	120.8(10)
N16	C8	S8	116.7(8)
N17	C9	S9	119.4(8)
N18	C9	S9	118.7(8)
N18	C9	N17	121.9(10)
N19	C10	S10	117.5(8)
N20	C10	S10	120.9(9)
N20	C10	N19	121.4(10)
N21	C11	S11	119.0(9)
N21	C11	N22	120.6(10)
N22	C11	S11	120.3(9)
N23	C12	S12	117.7(10)
N24	C12	S12	123.9(11)
N24	C12	N23	118.3(12)

Table S4 Areal and specific capacitance measured from CV under different scan rate (a) and from galvanostatic charge-discharge measurement under different specific current density (b).

a)

Scan rate / V s^{-1}	areal capacitance / mF cm^{-2}	specific capacitance / F g^{-1}	Electrode areal capacitance / mF cm^{-2}	Electrode specific capacitance / F g^{-1}
0.5	23.7	14.7	47.4	29.4
0.2	44.5	27.7	89	55.4
0.1	61.2	38.0	122.4	76
0.05	79.0	49.1	158	98.2
0.02	108	67.0	216	134
0.01	140	87.2	280	174.4

b)

specific current density / A g^{-1}	areal capacitance / mF cm^{-2}	Maximum specific capacitance / F g^{-1}	average specific capacitance / F g^{-1}	Maximum Electrode areal capacitance / mF cm^{-2}	Maximum Electrode specific capacitance / F g^{-1}
1.74	943	586	169	1886	1172
1.30	1060	656	178	2120	1312
0.87	1290	803	218	2580	1606
0.44	1660	1030	238	3320	2060
0.22	1450	899	348	2900	1798

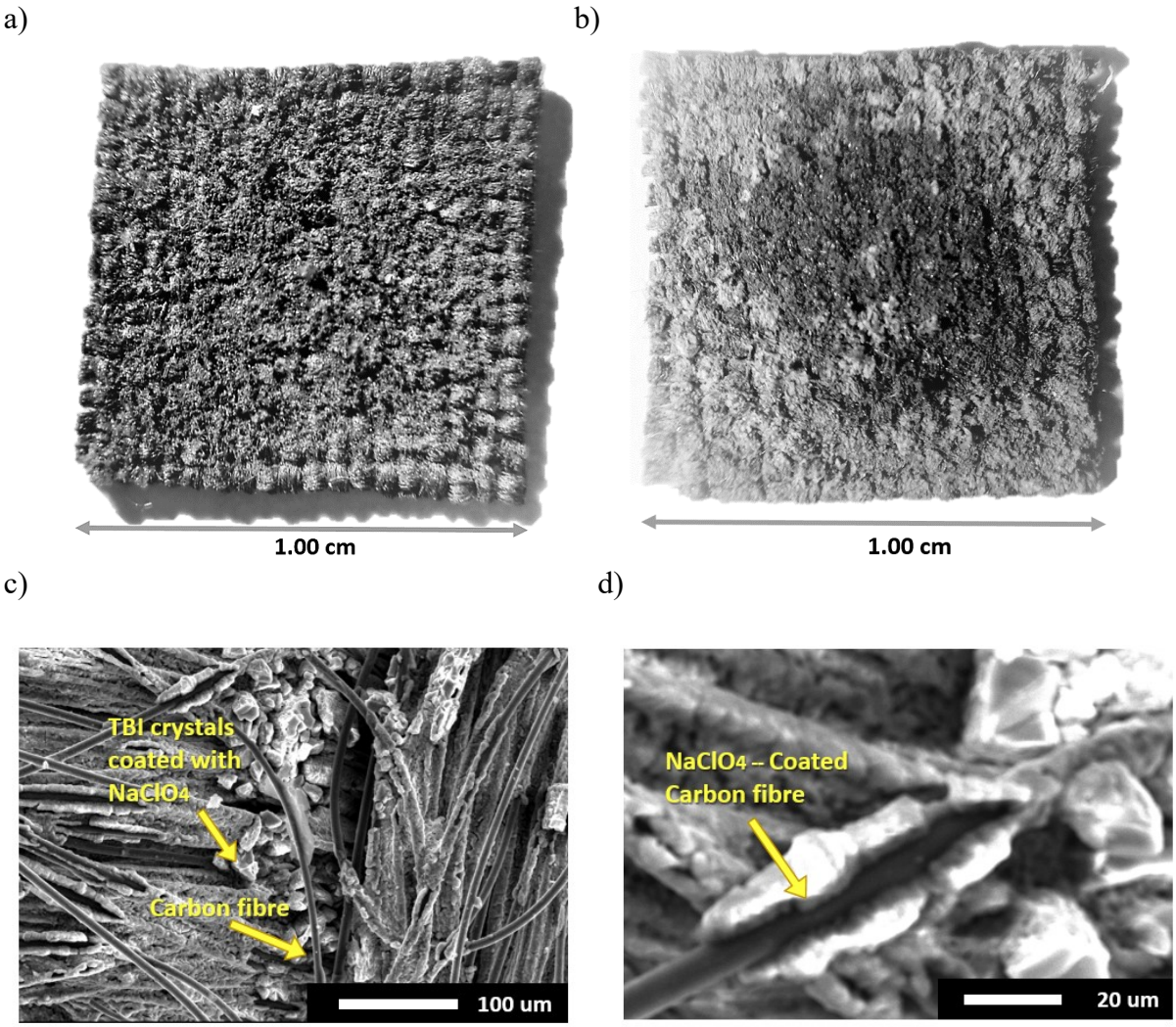

Figure S2. Pictures of as-deposited TBI/carbon cloth electrodes (a) before 5000 cycles and (b) after 5000 cycles, with contrast +50% and brightness +50%; SEM images of TBI/carbon cloth electrodes after 5000 cycles (c) (d), showing heavily-coated $NaClO_4$ electrolyte.

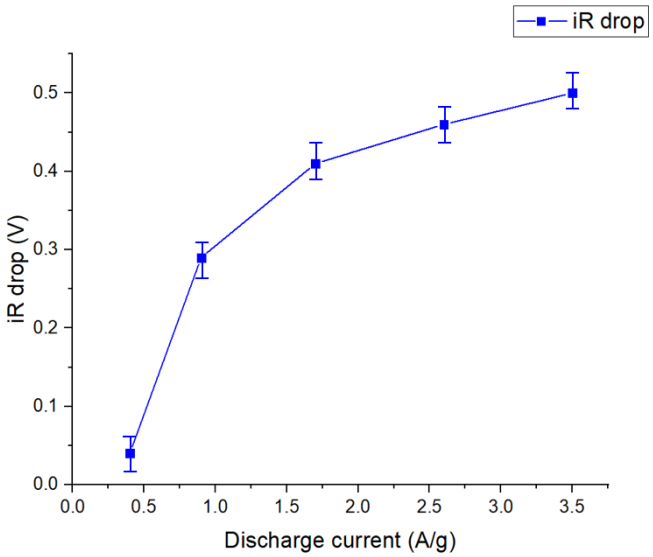

Figure S3. The relationship between iR loss (caused by internal resistance) and discharge current.

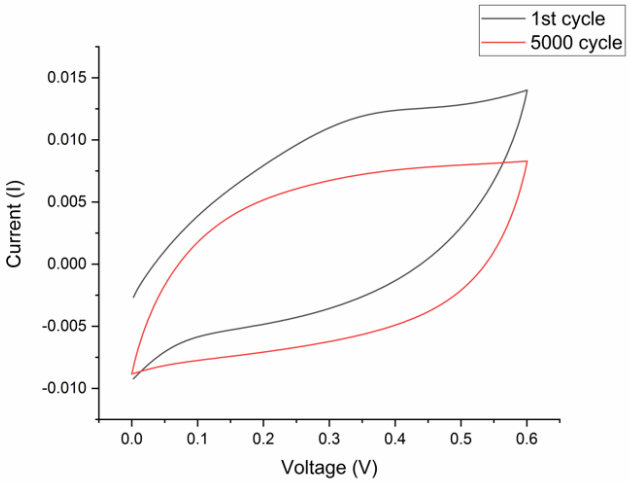

Figure S4. (a) CV curve of a TBI-based supercapacitor at its 1st cycle and 5000th cycle.

a)

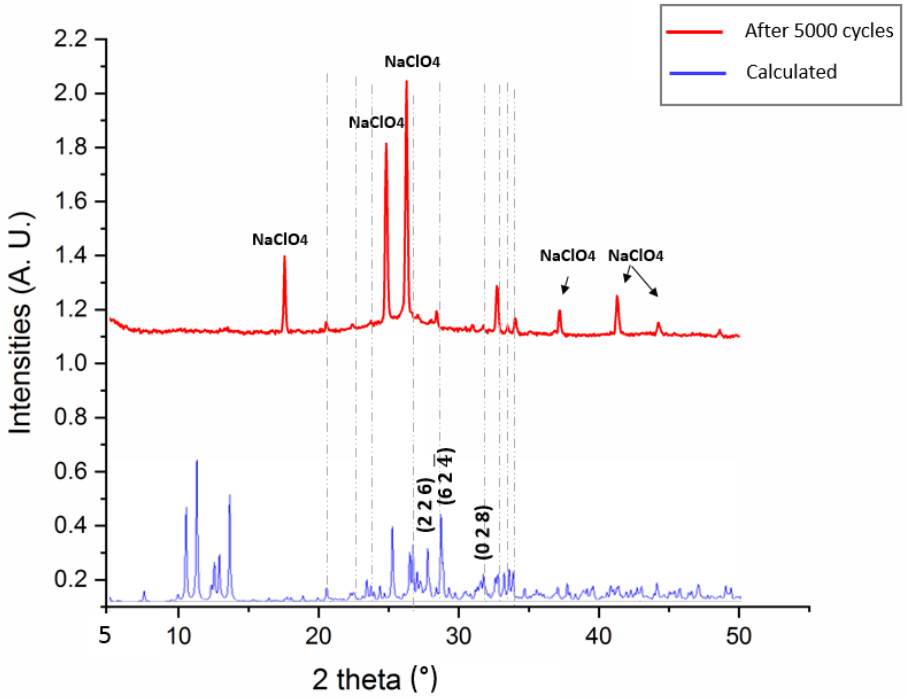

b)

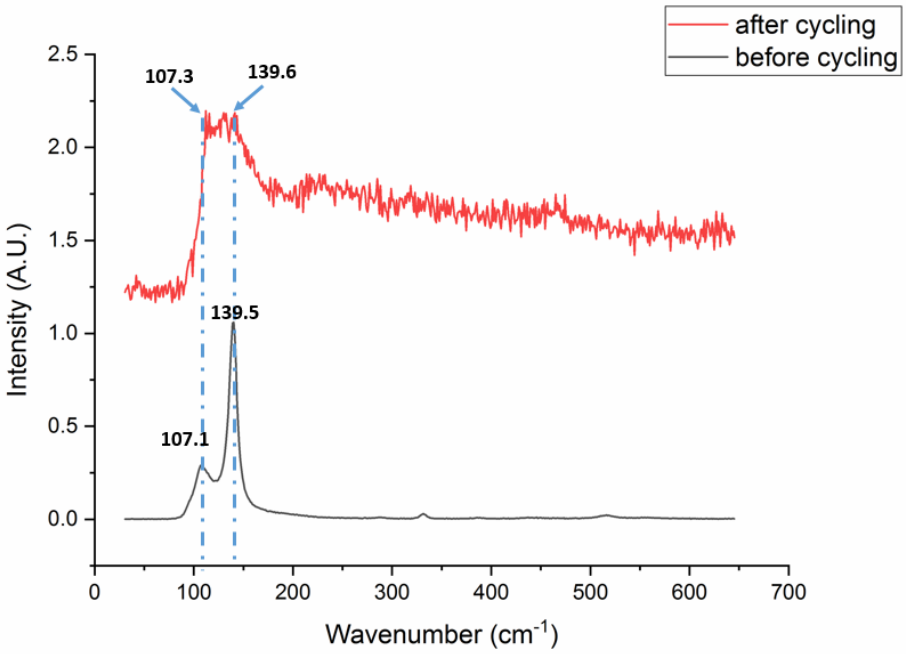

Figure S5. (a) Powder XRD pattern of TBI electrode after 5000 cycles compared (red) with the theoretical pattern (blue). (b) Raman spectra of as-prepared TBI electrode (black) and after 5000 cycling test (red).

a) b)

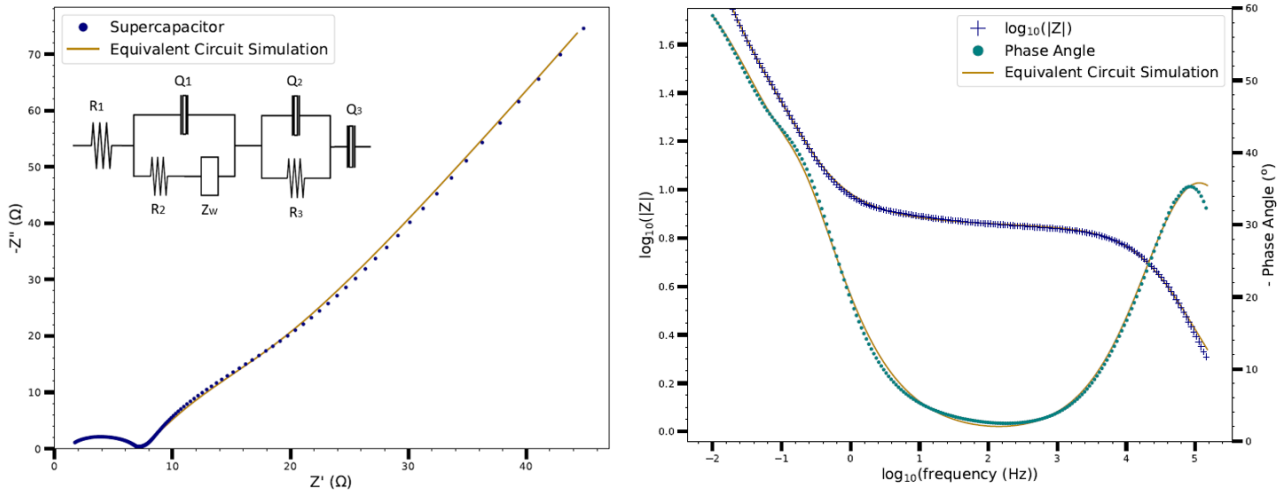

Figure S6. (a) Nyquist plot and (b) Bode plot of TBI-based supercapacitor after 5000 long-term cycle test, with simulated circuit and results inserted.

Table S5. The values for equivalent circuit elements in the simulated circuit for TBI-based supercapacitor measured after 5000 long-term cycle test

Circuit Element	Value	% Error
R_1	0.864 Ω	10.501
$Q_1 - n$	0.7496	1.503
$Q_1 - Y_0$	1.867 mF	11.023
R_2	6.27 Ω	1.634
$Q_2 - n$	1	3.272
$Q_2 - Y_0$	0.3571 F	8.072
R_3	3.58 Ω	9.135
$Q_3 - n$	0.7938	0.494
$Q_3 - Y_0$	0.1424 F	2.528
W1	0.2087 Ω^{-1} $s^{1/2}$	6.335

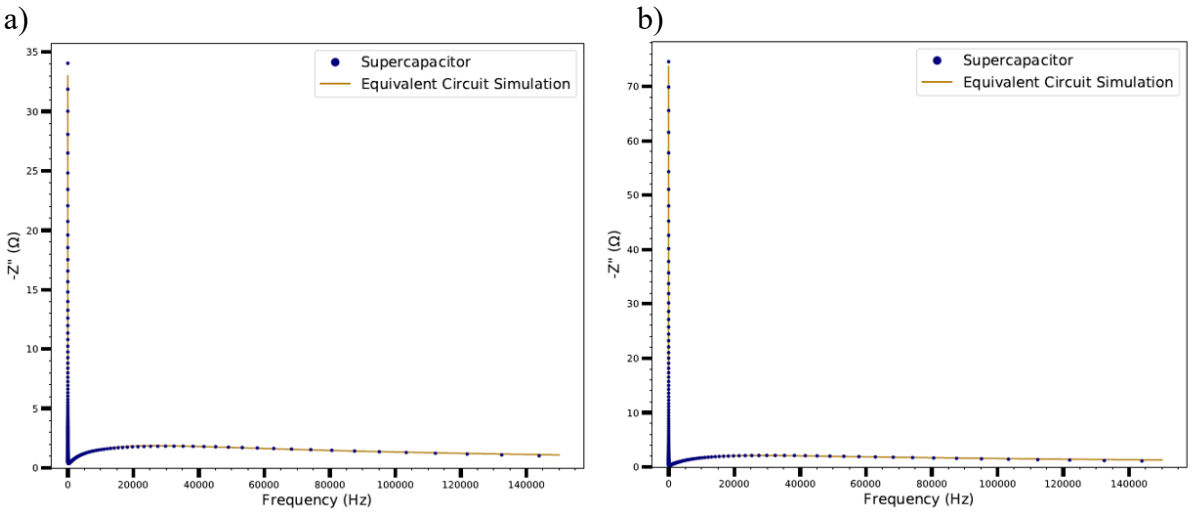

Figure S7. Frequency vs Z''before (a) and after (b) 5000 cycles